Medical Image Analysis 67 (2021) 101829

Contents lists available at ScienceDirect

Medical Image Analysis

journal homepage: www.elsevier.com/locate/media

Research paper

Statistical deformation reconstruction using multi-organ shape features for pancreatic cancer localization

Megumi Nakao[a,1,*], Mitsuhiro Nakamura[b,1], Takashi Mizowaki[c], Tetsuya Matsuda[a]

[a] Graduate School of Informatics, Kyoto University, Yoshida-Honmachi, Sakyo, Kyoto 606-8501, Japan
[b] Human Health Sciences, Graduate School of Medicine, Kyoto University, Shogoin-Kawahara-cho, Sakyo, Kyoto 606-8507, Japan
[c] Dept. of Radiation Oncology and Image-Applied Therapy, Kyoto University Hospital, Shogoin-Kawahara-cho, Sakyo, Kyoto 606-8507, Japan

ARTICLE INFO

Article history:
Received 15 February 2020
Revised 12 August 2020
Accepted 12 September 2020
Available online 10 October 2020

Keywords:
Statistical deformation library
Multi-organ motion analysis
Kernel modeling
Adaptive radiotherapy

ABSTRACT

Respiratory motion and the associated deformations of abdominal organs and tumors are essential information in clinical applications. However, inter- and intra-patient multi-organ deformations are complex and have not been statistically formulated, whereas single organ deformations have been widely studied. In this paper, we introduce a multi-organ deformation library and its application to deformation reconstruction based on the shape features of multiple abdominal organs. Statistical multi-organ motion/deformation models of the stomach, liver, left and right kidneys, and duodenum were generated by shape matching their region labels defined on four-dimensional computed tomography images. A total of 250 volumes were measured from 25 pancreatic cancer patients. This paper also proposes a per-region-based deformation learning using the non-linear kernel model to predict the displacement of pancreatic cancer for adaptive radiotherapy. The experimental results show that the proposed concept estimates deformations better than general per-patient-based learning models and achieves a clinically acceptable estimation error with a mean distance of 1.2 ± 0.7 mm and a Hausdorff distance of 4.2 ± 2.3 mm throughout the respiratory motion.

© 2020 The Author(s). Published by Elsevier B.V.
This is an open access article under the CC BY license (http://creativecommons.org/licenses/by/4.0/)

1. Introduction

Statistical formulation of respiratory motion including the deformation of multiple organs and tumors is of increasing interest in external-beam radiotherapy. Specifically, in image-guided radiotherapy (IGRT), it is important to reduce exposure in normal tissues while accurately targeting lesions with respiratory motion. However, large anatomical variations in the shape and motion of abdominal organs can occur when treatment lasts several weeks, while time-series three-dimensional (3D) computed tomography (CT) images can only be obtained for initial radiation planning (Rigaud et al., 2019; Magallon-Baro et al., 2019). Recent technical advances enable treatment plans to be modified based on a daily X-ray cone-beam CT (CBCT). This process is called adaptive radiotherapy (ART) (Posiewnik and Piotrowski, 2019; Hvid et al., 2018). Abdominal organs such as the stomach, and duodenum or the pancreas neighbor each other, but the pancreas cannot clearly be detected, even on CBCT images. Because missing pixel values or artifacts often appear in CBCT images (see Fig. 1), ART for abdominal regions is technically more difficult and remains a challenging area of research (Magallon-Baro et al., 2019; Posiewnik and Piotrowski, 2019). To approach these issues, this paper focuses on the potential of model-based tumor localization in pancreatic cancer treatment using statistical modeling of patient-specific multi-organ motion and deformation.

Statistical shape modeling (SSM) has been widely investigated for the modeling of organ shapes based on prior knowledge (Heimann and Meinzer, 2009; Soliman et al., 2017), and interest has grown in its application in machine learning with intra- or inter-patient datasets with point-to-point correspondence (Rigaud et al., 2019; Magallon-Baro et al., 2019; Nakamura et al., 2019; Tilly et al., 2017). For instance, interfractional shape variations in the prostate and rectum have been statistically modeled for radiation therapy planning (Nakamura et al., 2019; Haekal et al., 2018; Bondar et al., 2014). A statistical deformation model (Ehrhardt et al., 2011; Jud et al., 2017) based on a four-dimensional (4D) CT images has also been reported. Unlike physics-based modeling (Fuerst et al., 2015; Nakao and Minato, 2010; Nakao et al., 2007), statistical modeling is a data-driven approach that does not explicitly describe the elasticity and physical conditions of organs. Image-based

* Corresponding author.
E-mail address: megumi@i.kyoto-u.ac.jp (M. Nakao).
[1] M. Nakao and M. Nakamura contributed equally to this work.

https://doi.org/10.1016/j.media.2020.101829
1361-8415/© 2020 The Author(s). Published by Elsevier B.V. This is an open access article under the CC BY license (http://creativecommons.org/licenses/by/4.0/)

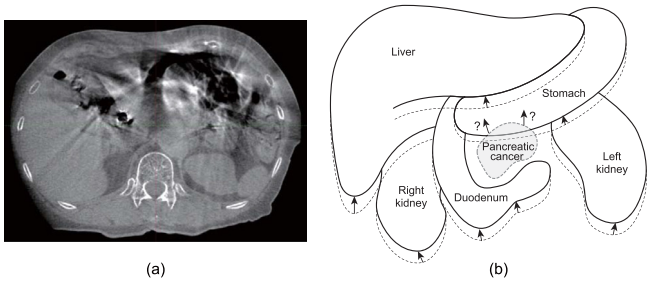

Fig. 1. Clinical needs for indirect deformation reconstruction in ART: (a) CBCT images with missing pixels and (b) a conceptual image of pancreatic cancer localization from multi-organ shape features.

(Sotiras et al., 2013; Ruhaak et al., 2017), point-based (Haekal et al., 2018; Shibayama et al., 2017), or mesh-based (Rigaud et al., 2019; Magallon-Baro et al., 2019; Nakamura et al., 2019; Nakao et al., 2019) deformable registration techniques have been used to obtain point-to-point correspondence between two datasets. Specifically, respiratory motion (Jud et al., 2017; Fuerst et al., 2015; Ruhaak et al., 2017; Wilms et al., 2016) has mainly been investigated in the field of image-based lung modeling.

Our aim in this paper is to statistically model inter- and intra-patient deformation along with the motion of multiple abdominal organs. The relationships among organs, especially those between pancreatic cancer and its surrounding organs, are also interesting and worth investigating (Yu et al., 2016; Fontana et al., 2016). Image-based registration assumes that the 3D image or the regions of interest of organs are a continuous space. It also assumes that the displacement is spatially smooth for regularization (Sotiras et al., 2013; Zhang and Chen, 2018; Oh and Kim, 2017; Klein et al., 2010). However, the mechanism for multi-organ deformation is complex and not fully understood. Respiratory motion widely affects abdominal regions, in which several organs are adjacent to or connected with each other. Therefore, to analyze individual motion and deformation accurately, a model capable of capturing sliding motion or rotation near the organ boundary is needed (Jud et al., 2017). Hence, interest in deformable mesh registration (DMR) has recently resurged. The inter- and intra-patient variations in cervix–uterus anatomy were recently modeled for radiation therapy planning (Rigaud et al., 2019; Tilly et al., 2017). The correlation of liver and pancreas tumor motion (Robert et al., 2017) and daily changes in the stomach, duodenum, and pancreas (Magallon-Baro et al., 2019) have been analyzed through DMR. To the best of our knowledge, there has been no report clarifying the relationship between the inter- and intra-patient deformations of multiple organs and tumors, even though the clinical needs for such modeling in radiotherapy and motion recognition are high (Jadon et al., 2014; Iwai et al., 2017; Teske et al., 2015; Whitfield et al., 2012).

In this paper, we introduce a localized deformation reconstruction framework based on the shape features of multiple organs. To model the relationships of the spatial deformation fields between abdominal organs and the tumor, a statistical multi-organ deformation library is constructed by shape matching organ meshes generated from 4D-CT datasets (250 volumes). We apply the developed library to estimate the motion and deformation of the pancreatic cancer through kernel regression. Five abdominal organs (the liver, stomach, duodenum, and right and left kidneys) located around the pancreas are used as multidimensional shape features. In such a procedure, a low number of cancer patients in the database can decrease the estimation performance, which is a common problem in clinical machine learning. To design the nonlinear kernel-based framework that maps the motion/deformation of pancreatic cancer and its surrounding organs, we address the following fundamental issues:

- We statistically investigate the level of complexity of the motion dynamics of multiple abdominal organs, their deformation, and relationships through DMR.
- We propose the concept of per-region, localized kernel learning for stable deformation estimation, rather than learning on a per-patient basis.
- We analyze which organ sets are good estimators for predicting the motion/deformation of gross tumor volume (GTV) and determine an appropriate number of dimensions for the feature space.
- We evaluate the final estimation performance for the inter- and intra-patient validation and address whether the proposed concept is clinically acceptable.

We note that the purpose of shape/deformation reconstruction is different from that of image segmentation, for which a variety of deep learning methods that directly use image features in the regions of interest have been proposed (Xu et al., 2019). The current difficulties of ART for pancreatic cancer lie in the few opportunities for directly identifying the GTV of the day. The influence of respiratory-associated deformation on the ART procedure is probably larger than that of daily gradual changes in the GTV's volume. In this paper, as shown in Fig. 1(b), we argue that the motion and deformation of the pancreatic cancer can be indirectly reconstructed from the multi-organ features of the surrounding "visible" organs, regardless of the size and shape of the tumor of the day, even if the pancreas is totally "invisible" because of missing pixels in CBCT images or motion artifacts in 4D-CT images. The developed indirect estimation framework helps optimize radiation treatment in that the radiation dose can be locally transported to the moving tumor while maintaining a safe margin around organs at risk.

2. Methods

2.1. Statistical multi-organ deformation model

In this study, 4D-CT images $I_t^{(k)}$ ($k = 1, 2, \ldots, 25$: patient ID, $t = 1, 2, \ldots, 10$: time phase of 4D-CT images) of 25 pancreatic cancer patients who underwent intensity-modulated radiotherapy (IMRT) in Kyoto University Hospital were used for statistical modeling and deformation learning. This study was performed in accordance with the Declaration of Helsinki and was approved by our institutional review board (approval number: R1446). 4D-CT images for a patient consisted of 3D-CT images (image size: 512 × 512 pixels and 88–152 slices, voxel resolution: 1.0 mm × 1.0 mm × 2.5 mm) of 10 time phases for one respiratory cycle. All images were measured under the condition of respiratory synchronization, where $t = 1$ corresponds to the end-inhalation phase and $t = 6$ corresponds to the end-exhalation phase.

The 3D labels of the organs at risk (OARs), which were manually outlined for dose calculation in the radiation planning, were used as the multi-organ shape database. In the daily clinical procedures in Kyoto University Hospital, the regions of the entire body, stomach, liver, duodenum, left and right kidneys, and the GTV of the pancreatic cancer are labelled by board-certified radiation oncologists, as shown in Fig. 2(a). We note that stable outlining is not clinically available for the stomach, duodenum, and pancreas because of their unclear boundaries, image contrasts, and air contents. In addition, this paper does not focus on automatic segmentation techniques. Because the labels were actually determined in radiotherapy procedures after clinical validation, we used them as ground-truth regions for the five organs and the GTV to build the multi-organ deformation library.

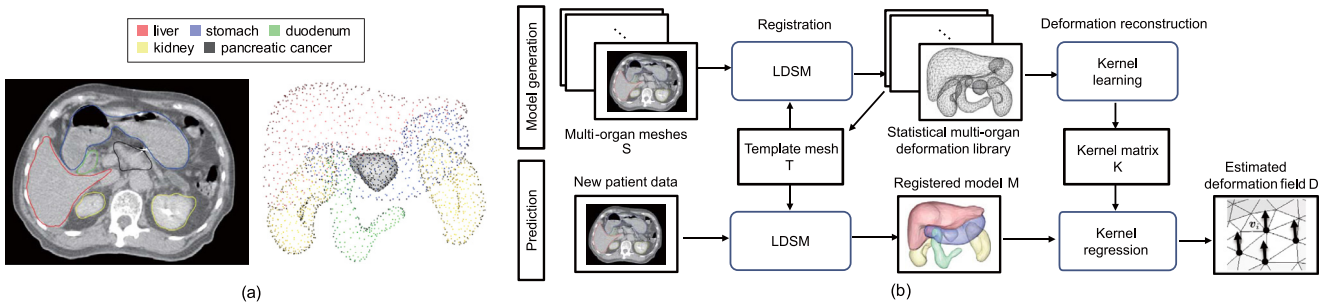

Fig. 2. Deformation reconstruction framework using the shape features of multiple abdominal organs. (a) CT slice image with the 3D contours of the liver, stomach, duodenum, left and right kidneys (left), and the GTV of pancreatic cancer along with the vertex distribution of the meshes (right). (b) Block diagram of the framework. The template meshes are registered to individual organ regions using Laplacian-based diffeomorphic shape matching (LDSM). The motion and deformation of pancreatic cancer are predicted from sparsely sampled multi-organ features using kernel regression.

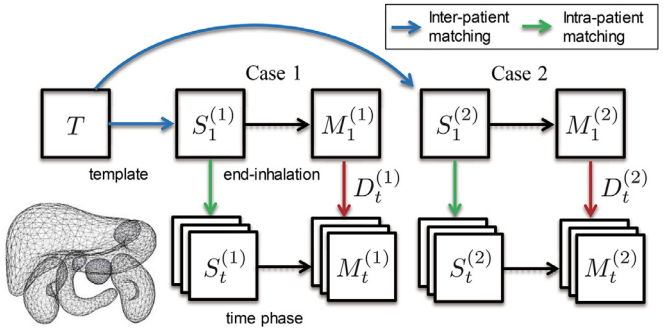

Fig. 3. Flow of the inter- and intra-patient shape matching. The spatial deformation D_t between the end-inhalation state and time phase t is obtained from the corresponding vertices of the two registered meshes.

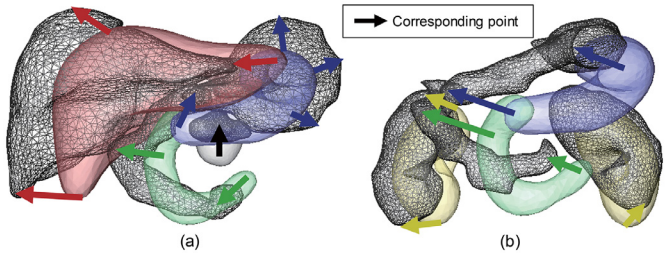

Fig. 4. Examples of complex inter-patient shape changes and the interactions among multiple abdominal organs. (a) A part of the liver and stomach deform in different directions near their boundaries (red and blue arrows). (b) The duodenum and right kidney do not contact each other in the template model, but are in contact in the patient models (green and yellow arrows). (For interpretation of the references to color in this figure legend, the reader is referred to the web version of this article.)

Fig. 2(a) shows an example of tetrahedral meshes $S_t^{(k)}$ and their volumetric point distribution for five organs and the GTV of the pancreatic cancer. (Table 1 summarizes the notations used in this paper.) Additionally, Fig. 2(b) shows the flow of the developed framework. The meshes of different organs (the liver, for instance) differ in the number of vertices and the structure of the mesh, because they were independently generated from different CT images. As shown in Fig. 3, the corresponding models $M_t^{(k)}$ (with the same vertex and the same mesh structure) that precisely approximate the surfaces of $S_t^{(k)}$, were computed by DMR using a template T and the target mesh. To address the trade-off between feature-preserving shape matching and spatially smooth deformation, DMR is performed by the proposed Laplacian-based diffeomorphic shape matching (LDSM), which is an extension to Laplacian-based shape matching (Kim et al., 2015). Because the registered models achieve point-to-point correspondence, spatial deformation $D_t^{(k)} = M_t^{(k)} - M_1^{(k)}$ can be represented by calculating the displacement vector of the corresponding vertex.

Table 1
Notation table

Symbol	Definition
t	time phase for 4D-CT
k	patient id
i, j	vertex id
$\boldsymbol{I}_t^{(k)}$	time series, 3D-CT volumes
$\boldsymbol{S}_t^{(k)}$	organ surfaces
$\boldsymbol{T}$	template mesh
$\boldsymbol{M}_t^{(k)}$	registered models (deformed templates)
$\boldsymbol{v}_i$	position of vertex
$\boldsymbol{u}_i$	displacement of vertex
$\boldsymbol{r}_{ij}$	relative position between vertex i and j
$\boldsymbol{x}_i$	feature vector
$\boldsymbol{y}_i$	estimated displacement vector

To stably compute a 3D deformation field of multiple organs, accurate shape matching is required. The shape variation and deformation of abdominal organs such as the stomach and duodenum include considerable volume changes including rotations and sliding boundaries. Fig. 4 shows examples of complex inter-patient shape changes and the interaction between multiple abdominal organs. A part of the liver and stomach deform in the different directions near their boundaries. The duodenum and right kidney do not contact each other in the template model, but are in contact in the patient models. Image-based registration generally deals with multiple organs as one continuous image space, and an individual organ's deformation or interactions among specific organs cannot be discriminated. In addition, the registration error tends to increase in areas with large curvature such as the tips of the organs and boundaries of neighboring organs (Jud et al., 2017; Nakao et al., 2019). Specifically, our focus in this paper is to model multi-organ motion/deformation and its interaction, and to examine the efficacy of the proposed feature-preserving registration methods for abdominal organs with large shape variations such as the stomach and duodenum. To capture rotational components or possible sliding motions caused by the interaction of multiple organs, the registration process is applied to each organ's mesh independently. In addition to intra-patient registration, our approach enables the construction of a statistical deformation model, making inter-patient deformation analysis possible. The details of the applied DMR method, LDSM, are described in Section 2.3.

For the template mesh generation, first, one case was randomly selected to be the initial shape for the template mesh T, and its surface was resampled to 400 vertices and 796 triangles. At this

point, the number of vertices was determined by qualitatively considering shape representation of the five organs and the GTV. The registration accuracy and final number of sampling points that are suitable for deformation reconstruction were investigated in the experiments. Next, the corresponding mesh models $M_t^{(k)}$ were obtained by registering T to the individual surfaces $S_t^{(k)}$. Because the mesh models $M_t^{(k)}$ have point-to-point correspondence, the average shape $\overline{M}$ can be obtained by calculating the average of each coordinate. We used $\overline{M}$ as the final template. This process was performed on the stomach, liver, left and right kidneys, and duodenum. By keeping the template close to the data in advance, our aim is to reduce the influence of the adopted data selection while preventing an increase in matching error. The efficacy of this template setting has been confirmed in a variety of organs in past studies (Nakamura et al., 2019; Nakao et al., 2019).

2.2. Localized deformation learning model

To learn respiratory motion/deformation, the end-inhalation phase ($t = 1$) of 4D-CT images is used as the initial patient anatomy. In the clinical setting, this information is obtained from a 3D-CT measured for radiotherapy planning. All remaining data ($t = 2, 3, \ldots, 10$) are used for kernel learning in one batch without separating them by time. In the prediction stage, the time-varying position of the pancreatic cancer is estimated using the kernel function and the multi-organ features. No information about the time phase is needed for this prediction. In other words, the 4D-CT database is used to statistically learn the variation in respiratory deformation, and the time phase and its continuity are utilized in neither training nor prediction. Because tumor localization can be achieved statically regardless of the time evolution, stable estimation is possible without error accumulation even if irregular respiration occurs during treatment.

In our framework, complete anatomical contours of the CBCT images are not needed for GTV prediction during treatment. It is designed to predict the motion/deformation of GTV from partly observed anatomical features in the CBCT images available during daily treatment over time. We hypothesize that the small parts of shapes or contours detectable from the CBCT images are sufficient for this prediction. For instance, local textures or some corresponding points of the surrounding organs are the candidates of the available feature sets. The experiments were designed to clarify which feature sets are effective for predicting GTV.

As the second technical challenge, we introduce the localized multi-organ features for modeling inter- and intra-patient variation of deformation from a dataset containing a limited number of patients. To model spatial deformation, per-patient-based learning, in which one patient's data are used as one set of training data, has been generally employed as a straightforward approach. Instead of reconstruction on a per-patient basis, the aim of this paper is to formulate a method for local deformation reconstruction that models nonlinear motion for a small region of the estimation target. In the proposed learning model, a small local region of the target organ is used as one set of training data. This approach is based on the hypothesis that local regions with similar shape features show similar displacements, which is commonly assumed in each continuous space of organs.

The difference in the proposed per-region based deformation learning is twofold: (1) the ability to reconstruct shape variations and (2) the stability of learning obtained by separating the training datasets into small regions. In traditional per-patient based deformation learning, because the organ shapes are globally modeled or controlled, shape representations are limited to the number of patient data m. In contrast, in the proposed per-region based deformation learning, organ shapes are locally modeled per each small region of curved surfaces. More shape variations can be reconstructed by learning the relationship between the local shape features and the deformation. The stability of learning should also improve because the number of training units is greatly increased by separating the organ shapes into small regions. In this approach, the number of training data is $m \times n$ when the number of patients in the data is m and n small regions of the target organ are considered. The details of the deformation reconstruction framework is described in Section 2.4.

2.3. Feature preserving deformable mesh registration

In this study, to achieve both globally stable and locally strict DMR, our aim is to address the trade-off between feature-preserving shape matching and spatially smooth deformation. To approach this in DMR, the concept of progressive, feature-preserving shape update (Nakao et al., 2019; Kim et al., 2015) is introduced into the large deformation diffeomorphic metric mapping (LDDMM) scheme (Zhang and Chen, 2018; Beg et al., 2005). The objective function in the proposed LDSM is described as follows.

$$E(\boldsymbol{u}) = d(Y, \phi(X)) + \int_0^1 \|L(\boldsymbol{u}(s))\|^2 ds, \tag{1}$$

where X is the source (template) mesh, Y is the target surface, and d is the distance function between the two surfaces. In addition, $\phi(X)$ is a continuous and differentiable transformation that maps X to the deformed mesh, $L(\ \cdot\ )$ is the Laplace–Beltrami operator and $L(\boldsymbol{u})$ is the discrete Laplacian of the displacement field.

The first term evaluates the difference between the deformed template and the target surface. The second is a regularization term to make the deformation field \boldmath u smooth. In the context of image-based LDDMM, the difference in voxel intensities between the deformed and the target image is evaluated in the first term. Minimizing the nearest point-to-point distance was originally employed as a basic strategy in DMR, however, it does not consider 3D geometry, and maintaining mesh topology is difficult with this approach. We focus on the importance of feature preservation to avoid incorrectly matching local structures (Nakao et al., 2019) in mapping distant structures, 3D geometric information of the template mesh is used to preserve the local features of organ shapes. In the mapping function ϕ, a Laplacian-based shape matching (LSM) scheme (Kim et al., 2015) is introduced for progressive shape updates while preserving features as much as possible. The mean value of the nearest bidirectional point-to-surface distance (called the mean distance in this paper) is used for d. A discrete Laplacian was first formulated for geometry modeling (Nealen et al., 2006), and has recently been applied to the non-rigid shape registration of anatomical structures (Nakao et al., 2019; Kim et al., 2015). In Kim et al. (2015), LSM registers curved surfaces with shape variations better than LDDMM.

Let X denote a tetrahedral mesh with n vertices $\boldsymbol{v}_i \in V (i = 1, 2, \ldots, n)$ and edges, the deformation map $\phi(X)$, that is, the deformation field $\boldsymbol{u}$ in the LSM, is obtained by iteratively updating $\boldsymbol{v}_i$ while minimizing the following objective function:

$$\begin{aligned} E(\boldsymbol{u}) &= E_{shape} + \delta E_{pos} \\ &= \sum_{i=1}^{n} \|L(\boldsymbol{v}_i') - L(\boldsymbol{v}_i)\|^2 + \delta \sum_{i=1}^{n} \|\boldsymbol{p}_i - \boldsymbol{v}_i\|^2, \end{aligned} \tag{2}$$

where $\boldsymbol{v}_i'$ is the vertex position to be solved, $\boldsymbol{p}_i$ is a positional constraint set to $\boldsymbol{v}_i$, and δ is a weight parameter configured according to the problem. The positional constraint $\boldsymbol{p}_i$ is determined as an internal division point of the smoothed position and its projected position on the target tangent plane. For the details of the definition of the positional constraints between the template and target

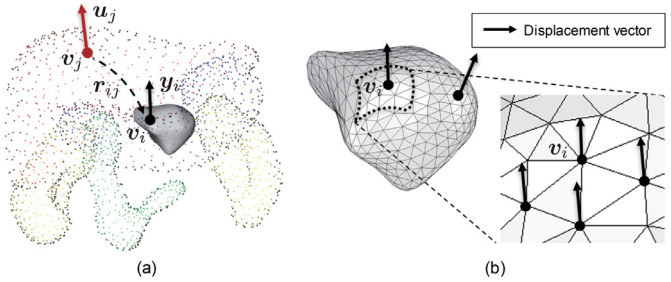

Fig. 5. Per-region-based localized deformation learning: (a) a displacement mapping model, and (b) deformation learning by considering the continuity of spatial deformation.

shape, refer to Nakao et al. (2019). $L(\boldsymbol{v}_i)$ is the discrete Laplacian at vertex $\boldsymbol{v}_i$, defined by

$$L(\boldsymbol{v}_i) = \sum_{j \in V_i} \omega_{ij}(\boldsymbol{v}_i - \boldsymbol{v}_j) \tag{3}$$

Here, ω_{ij} are the edge weights and V_i is the set of adjacent vertices of one ring connected by vertex $\boldsymbol{v}_i$ and the edge. The discrete Laplacian is used as a shape descriptor and approximates the mean curvature normal of the triangular mesh. Although there are several variations of the weights, the general one is cotangent discretization based on the per-edge Voronoi areas. The first term in Eq. (2) is a penalty for shape changes to the mesh, and the second term increases if the constrained vertex is distant from the nearest surface of the target mesh. By computing $\boldsymbol{v}_i'$, which minimizes the objective function, the template model is updated while preserving the shape as much as possible.

In the proposed LDSM, in addition to LSM, the regularization term in Eq. (1) is used to achieve a spatially smooth and diffeomorphic deformation. This can be simply implemented by adding the term to Eq. (2) as follows:

$$E(\boldsymbol{u}) = E_{shape} + E_{deform} + \delta E_{pos} \tag{4}$$

where E_{deform} is the magnitude of the discrete Laplacian of the deformation field $\boldsymbol{u}$ defined by

$$E_{deform} = \sum_{i=1}^{n} \|L(\boldsymbol{u}_i)\|^2 \tag{5}$$

Because Eq. (5) is a quadratic form at vertex positions $\boldsymbol{v}_i$, this minimization problem can be computed in a short time by solving linear equation (Nealen et al., 2006). The step-by-step update avoids local mismatches at the early stage if there is a considerable distance between the two surfaces. Once the template is updated, local displacement $\boldsymbol{u}_i = \boldsymbol{v}_i' - \boldsymbol{v}_i$ is obtained. We note that the original LDDMM does not preserve the shape of the template, and some studies report results with unstable or irregular matching especially for large deformations with rotation (Nakao et al., 2019; Kim et al., 2015). In the proposed framework, in addition to the regularization term, Laplacian-based shape preservation is introduced into the iterative deformation process.

2.4. Localized kernel for deformation reconstruction

This section explains the per-region-based localized deformation learning proposed in this paper, by comparing it with the per-patient-based deformation learning generally used in population-based modeling (Rigaud et al., 2019; Nakamura et al., 2019). Fig. 5 briefly illustrates the concept. Because the aim of this paper is to reconstruct target deformation from multi-organ features, the displacement vector $\boldsymbol{y}_i$ is mapped from multiple points sampled from the surrounding organs, as shown in Fig. 5(a). We hypothesize that the local displacement $\boldsymbol{y}_i$ of GTV can be calculated from the feature vectors $\boldsymbol{x}_j$ of the vertices $\boldsymbol{v}_j$ that are sparsely sampled from the surrounded organs. In this paper, feature vector $\boldsymbol{x}_j$ is constructed using the relative position $\boldsymbol{r}_{ij}$ and displacement $\boldsymbol{u}_j$ of the sampled vertex.

Here, the problem is to learn the mapping from the registered multi-organ models generated through DMR. We assume that each vertex of the registered mesh models represent the intrinsic local region of the organs. Per-patient-based learning is a straightforward approach in which the mesh model M obtained from one patient's data is used as one set of training data. This approach is based on the idea that the displacement in the local regions of organs is similar to that of the corresponding regions of the training dataset with similar shape features. The displacement $\boldsymbol{u}_i$ at vertex i is learned from the displacement $\boldsymbol{u}_i$ of the corresponding vertex $\boldsymbol{v}_i$ in other cases. However, in per-region-based localized deformation learning, a small region Ω_i of the mesh model M is used as one set of training data. This approach is based on the idea that the two local regions in the target shape (i.e. GTV) that are close each other show similar displacement because the target surface is generally assumed to be a smooth curved manifold. For instance, in Fig. 5(b), the displacement vectors $\boldsymbol{u}_j$ adjacent to $\boldsymbol{v}_i$ are similar to those of $\boldsymbol{v}_i$. In other words, the displacement $\boldsymbol{u}_i$ can be learned from the displacement $\boldsymbol{u}_j$ of all vertices $\boldsymbol{v}_j$ in other cases.

We formulate the per-region-based deformation learning model using kernel functions. Based on the spatial mapping in Fig. 5(a), the local displacement $\boldsymbol{y}_i$ of GTV is computed from multi-organ shape features $\boldsymbol{x}_i$ using Eq. (6).

$$\boldsymbol{y}_i = \sum_{j=1}^{N} \boldsymbol{\alpha}_j k(\boldsymbol{x}_i, \boldsymbol{x}_j), \quad \boldsymbol{x}_j \in X, \quad \boldsymbol{\alpha}_j \in \mathbb{R}^N \tag{6}$$

where $k : X \times X \to \mathbb{R}$ is the kernel function defined for scalar component of the 3D displacement vector, N is the number of training datasets, and $\boldsymbol{\alpha}_j$ is the weight vector. A Gaussian function is used for kernel function k, which is $k(\boldsymbol{x}_i, \boldsymbol{x}_j) = exp(-\beta||\boldsymbol{x}_i - \boldsymbol{x}_j||^2/N)$. For a given $\boldsymbol{y} = [\boldsymbol{y}_1, \ldots, \boldsymbol{y}_N]^T$, $\boldsymbol{\alpha} = [\boldsymbol{\alpha}_1, \ldots, \boldsymbol{\alpha}_N]^T$ are calculated by minimizing the cost function E(\boldmath α), which is expressed as

$$E(\boldsymbol{\alpha}) = \|\boldsymbol{y} - K\boldsymbol{\alpha}\|^2 + \lambda \boldsymbol{\alpha}^T K \boldsymbol{\alpha} \tag{7}$$

where $K \in \mathbb{R}^{N \times N}$ is the kernel matrix whose elements are defined by $K_{ij} = k(\boldsymbol{x}_i, \boldsymbol{x}_j)$, and λ is the regularization parameter, which penalizes deviations of $\boldsymbol{\alpha}$. The optimized weights are given by $\boldsymbol{\alpha} = (K + \lambda I)^{-1}\boldsymbol{y}$ (I: indentity matrix).

The feature vector $\boldsymbol{x}_i$ of the local region for per-region-based learning is constructed using the relative position $\boldsymbol{r}_{ij}$ of the target vertex and the displacement vector $\boldsymbol{u}_j$ of the surrounding organs as follows.

$$\boldsymbol{x}_i = [\boldsymbol{r}_{ij}, \boldsymbol{u}_j], \quad \boldsymbol{r}_{ij} = \boldsymbol{v}_i - \boldsymbol{v}_j \tag{8}$$

In this study, the sampled vertices obtained from 24 patients were used in leave-one-out cross-validation to construct the kernel matrix, and all vertices of the five organs (liver, left and right kidneys, stomach, and duodenum) were considered as candidates for shape features $\boldsymbol{x}$.

$$\boldsymbol{x}_{ALL} = [\boldsymbol{x}_{ST}, \boldsymbol{x}_{DU}, \boldsymbol{x}_{LI}, \boldsymbol{x}_{LK}, \boldsymbol{x}_{RK}] \tag{9}$$

where ST, DU, LI, LK, and RK are the stomach, duodenum, liver, left kidney, and right kidney, respectively. For instance, when 50 vertices are sampled from each organ model, the dimension of the feature vector $\boldsymbol{x}_i$ is 1500 according to $\boldsymbol{r}_{ij}, \boldsymbol{u}_j \in \mathbb{R}^{750}$. Because the shape features are evaluated in high-dimensional feature space, in per-patient-based deformation reconstruction, the estimation error may increase if there are no corresponding vertices with similar characteristics among the 24 cases.

Alternatively, in the proposed per-region-based deformation learning, the displacement is locally learned per vertex; in other

words, it can be reconstructed from the deformation of different regions. Therefore, when 200 vertices are used to represent the target pancreatic cancer (for example), the training dataset is substantially increased to $24 \times 200 = 4800$, whereas the number of dimensions of the feature space is 1500, which is the same as that of per-patient-based approach. This means that the number of neighborhood data points increase in the generated feature space, and the displacement of the target vertex can be reconstructed using more datasets. Therefore, using a per-region-based kernel formulation improves the estimation performance and more stable results can be expected.

As described in the introduction, we are interested in the following questions: which organ sets are good estimators for deformation reconstruction and what number of dimensions of the feature space is appropriate. Fig. 6 shows two examples in which the three vertices are mapped to the target vertex, which is a problem of obtaining the target displacement based on features sampled from different organ sets, $[\boldsymbol{x}_{LI}]$ from the liver or $[\boldsymbol{x}_{ST}, \boldsymbol{x}_{DU}]$ from the stomach and duodenum. The liver does not have clear anatomical connectivity to the pancreas, and the shape feature is relatively stable with a small deformation. The stomach and duodenum are connected to the pancreas, but their deformation is large (Magallon-Baro et al., 2019) and unstable. Because the shape features of all organs are not always obtained from CBCT images, to explore the prediction performance when using specific organ sets is worth investigating for clinical application. In general, when using higher dimensions for shape features, more shape variations and complex deformations can be modeled, but calculation cost increases and the contribution of each feature to the final estimation results is reduced. Because the appropriate dimensions of the feature vectors are problem-specific, we explore the estimation performance for different dimensions in the experiments, and investigate the possible organ sets for localizing pancreatic cancer.

3. Experiments

In the experiments, statistical multi-organ deformation models were first generated by inter- and intra-patient shape matching. The registration performance for each organ was confirmed while comparing it with the results from three existing registration methods. Then, the efficacy of the multi-organ shape features in predicting the motion and deformation of pancreatic cancer was analyzed. The performance of the proposed per-region-based deformation learning was evaluated by comparing it with conventional per-patient-based learning. The value of weight parameter β for kernel function was determined from the results of numerical experiments.

The overall framework was implemented using Visual C/C++, OpenGL, and the Intel Math Kernel Library. A computer with a graphics processing unit (CPU: Intel Core i7 3.7 GHz, Memory: 64 GB, GPU: NVIDIA GeForce GTX 2080Ti) was used throughout the experiments. Regarding the regularization parameters, we used 10.0 for δ and 0.1 for λ after the examination of several parameters sets.

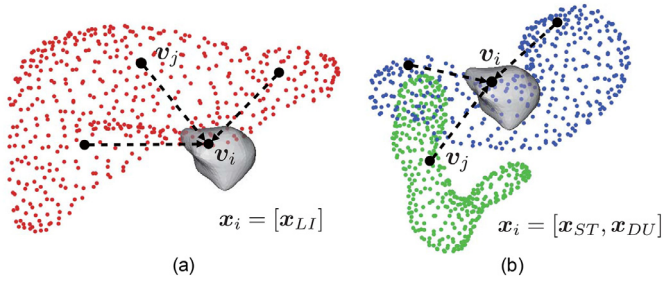

Fig. 6. Examples of displacement mapping models using multi-organ shape features. (a) Shape features sampled from the liver and (b) from the stomach and duodenum.

3.1. Shape matching performance

In this study, the mean distance (MD) (Rigaud et al., 2019; Kim et al., 2015), the Hausdorff distance (HD) (Huttenlocher et al., 1993), Laplacian of the displacement (LD) (Nakao et al., 2019) and Dice similarity coefficient (DSC) were used as the shape similarity criteria. MD and HD measure geometric distance, and DSC measures the volume overlap between the deformed meshes and the ground truth meshes. The Hausdorff distance measures the longest distance between two surfaces, whereas the mean distance is the mean value of the nearest bidirectional point-to-surface distance.

Unlike segmentation or recognition problems, statistical modeling requires point-to-point local correspondence between two shapes. For example, because the Dice coefficient only measures volume overlap, it is not suitable for evaluating per-region correspondence, nor is it suitable for measuring the quality of local matching. To identify unique/distinctive shape features specifically for the stomach and duodenum is very difficult because their shapes consist of smooth curved surfaces and substantially vary among patients. Therefore, we use the Laplacian of displacement as additional evaluation criteria. LD is the magnitude of the second derivative of the displacement field, and it evaluates the smoothness of registration. If shape features and vertex density are well preserved in DMR, this value decreases. The registered results with smaller MD, HD and LD values achieve the correspondence of local shapes.

The proposed shape matching method (LDSM) was compared with three existing shape matching approaches, that is,

- Piecewise Affine Transformation (PWA) (Pitiot et al., 2006; Zhou et al., 2010)
- Large deformation diffeomorphic metric matching (LDDMM) (Beg et al., 2005)
- Laplacian-based shape matching (LSM) (Kim et al., 2015; Saito et al., 2015)

For all algorithms, the affine transformation was processed in advance to match the posture and volume of the overall shape globally. To confirm the initial difference and complexity of intra-/inter-patient matching of abdominal organs, we also listed the geometric errors of rigid and affine registration (AF) results.

Table 2 shows the quantitative comparison results of the DMR algorithms for each of the five organs. The HD errors of rigid and affine registration are more than 12 mm, and large errors remain in the stomach and duodenum. LDSM and LSM achieved a significantly smaller mean distance and Hausdorff distance with an error of less than 1 mm, which shows better performance than PWA and LDDMM in terms of matching organs' shapes. There are no significant differences on the two distance metrics of LSM and LDSM (one-way analysis of variance, ANOVA; $p < 0.05$ significance level). Regarding the Laplacian of the displacement field, LDSM obtained smaller values than LSM, indicating that smooth deformation that reduces unstable surface matching can be performed by LDSM. In DMR, the accuracy of shape representation and smooth deformation from the template is a trade-off. Using the LDSM method, the Hausdorff distance is less than 1 mm (not significantly different compared to that of LSM), and the Laplacian of displacement is better than that of LSM. Based on these results, we selected the LDSM for constructing the deformation library of the five organs.

Table 2
Quantitative comparison results: mean distance (MD), Hausdorff distance (HD), mean and maximum Laplacian of the displacement (LD), and Dice similarity coefficient (DSC) of the DMR algorithms for the five organs. The values are shown as mean (minimum and maximum).

Liver	Methods					
	Rigid	AF	PWA	LDDMM	LSM	LDSM
MD [mm]	6.2 (3.4–11.6)	4.7 (2.9–8.5)	1.6 (1.1–2.4)	0.5 (0.3–0.7)	0.2 (0.1–0.3)	0.2 (0.1–0.3)
HD [mm]	22.1 (13.9–44.8)	19.0 (10.0–37.5)	10.0 (4.7.–28.7)	3.6 (1.3–14.8)	0.9 (0.4–1.9)	1.1 (0.5–2.2)
LD (mean) [mm]		2.4 (1.1–4.5)	2.3 (1.0–4.6)	1.1 (0.8–1.6)	1.5 (1.0–2.2)	1.2 (0.8–1.7)
LD (max) [mm]		12.7 (5.3–25.3)	12.0 (4.6–26.9)	6.8 (3.6–13.3)	8.8 (4.4–20.6)	7.0 (3.7–15.2)
DSC [%]	82.2 (68.9–90.8)	86.5 (76.3–92.0)	95.7 (92.4–97.2)	98.0 (96.1–98.6)	98.1 (96.1–98.7)	98.1 (96.1–98.7)
Stomach	Methods					
	Rigid	AF	PWA	LDDMM	LSM	LDSM
MD [mm]	5.6 (3.2–10.0)	4.4 (2.6–9.7)	1.4 (0.9–2.1)	0.5 (0.2–1.1)	0.2 (0.1–0.3)	0.2 (0.1–0.4)
HD [mm]	21.5 (10.0–53.5)	17.5 (9.3 –39.2)	7.3 (3.7–14.9)	3.1 (1.3–10.4)	0.8 (0.3–1.9)	0.9 (0.4–1.8)
LD (mean) [mm]		2.0 (0.5–5.4)	2.1 (0.8–5.0)	1.1 (0.7–2.0)	1.3 (0.8–2.5)	1.1 (0.6–2.0)
LD (max) [mm]		6.8 (1.7–18.2)	8.7 (3.6–43.2)	6.3 (3.0–10.8)	7.7 (3.9–15.7)	6.6 (2.9–12.2)
DSC [%]	69.5 (51.5–82.4)	75.0 (54.2–85.7)	92.6 (89.4–95.6)	96.5 (95.3–97.5)	97.2 (96.0–98.1)	97.0 (95.7–98.2)
Duodenum	Methods					
	Rigid	AF	PWA	LDDMM	LSM	LDSM
MD [mm]	4.7 (2.9–7.7)	3.8 (1.8–7.2)	1.2 (0.7–2.9)	0.5 (0.3–1.4)	0.2 (0.1–0.5)	0.2 (0.1–0.5)
HD [mm]	19.2 (9.0–38.2)	17.0 (7.4–40.4)	6.7 (2.9–23.0)	3.6 (0.8–13.1)	0.8 (0.3–4.2)	0.9 (0.4–5.0)
LD (mean) [mm]		1.1 (0.4–2.7)	1.5 (0.6–2.6)	1.0 (0.6–2.1)	1.2 (0.6–2.9)	1.0 (0.6–2.3)
LD (max) [mm]		3.5 (1.0–9.5)	6.6 (2.2–16.3)	6.9 (3.0–26.8)	7.8 (2.9–28.6)	7.2 (2.9–22.5)
DSC [%]	56.7 (29.9–72.6)	64.0 (28.5–80.8)	86.9 (54.1–92.6)	93.1 (70.6–96.4)	94.2 (69.0–97.4)	94.2 (72.2–97.2)
Left kidney	Methods					
	Rigid	AF	PWA	LDDMM	LSM	LDSM
MD [mm]	3.6 (1.9–6.8)	2.8 (1.5–6.1)	0.8 (0.6–1.2)	0.3 (0.2–0.9)	0.1 (0.1–0.2)	0.1 (0.1–0.3)
HD [mm]	13.1 (5.5–27.6)	12.3 (5.5–27.6)	4.8 (2.7–9.4)	2.8 (0.7–16.4)	0.5 (0.2–1.8)	0.7 (0.2–2.1)
LD (mean) [mm]		1.5 (0.5–2.5)	1.7 (0.7–4.1)	0.9 (0.5–2.2)	1.2 (0.6–2.9)	1.0 (0.5–2.3)
LD (max) [mm]		5.0 (1.7–10.8)	7.5 (2.6–21.7)	6.9 (3.1–15.4)	7.8 (3.0–24.6)	7.2 (2.6–21.7)
DSC [%]	81.0 (65.4–90.1)	86.0 (76.4–92.9)	95.9 (90.0–96.9)	97.2 (95.9–98.4)	97.4 (96.0–98.4)	97.4 (95.9–98.5)
Right kidney	Methods					
	Rigid	AF	PWA	LDDMM	LSM	LDSM
MD [mm]	3.5 (1.6–6.4)	2.8 (1.3–6.1)	0.8 (0.6–1.0)	0.3 (0.2–1.0)	0.1 (0.1–0.2)	0.1 (0.1–0.3)
HD [mm]	12.7 (5.9–25.9)	12.0 (4.8–24.6)	4.3 (2.4–9.1)	2.9 (0.5–13.1)	0.4 (0.2–0.9)	0.6 (0.3–2.0)
LD (mean) [mm]		1.4 (0.3–4.5)	1.6 (0.7–3.1)	0.8 (0.4–1.6)	1.0 (0.5–2.0)	0.8 (0.5–1.6)
LD (max) [mm]		4.7 (1.6–5.9)	8.6 (2.7–20.9)	6.9 (2.7–14.5)	8.1 (2.9–23.1)	7.0 (2.7–21.6)
DSC [%]	82.8 (67.2–92.1)	87.0 (73.2–93.6)	96.2 (94.8–97.3)	97.4 (96.3–97.9)	97.7 (96.6–98.6)	97.6 (96.4–98.4)

3.2. Multi-organ deformation analysis

So far, no study has investigated the impact of inter- and intra-subject variation on abdominal multi-organ deformation. Our DMR framework can directly provide a statistical representation of the registered organ models $M_t^{(k)}$, which can then generate the mean and variation of respiratory motion/deformation between subjects.

3.2.1. Statistical motion dynamics

Fig. 7 shows the statistical motion dynamics with deformation computed from registered organ models for ten time phases in one respiratory cycle. The mean displacement for all corresponding vertices are visualized as the centerline, and the standard deviation is depicted as a colored band. The graph shows that the mean and standard deviation of the displacement at the end-expiration phase is 12.1 $\pm$ 7.2 mm for the liver, 10.3 $\pm$ 5.5 mm for the stomach, 10.2 $\pm$ 5.9 mm for the duodenum, 11.4 $\pm$ 6.2 mm for the left kidney, 13.8 $\pm$ 8.4 mm for the right kidney, and 7.6 $\pm$ 4.2 mm for the GTV of the pancreatic cancer. The standard deviation is relatively large compared with the magnitude of the displacement. This indicates that there are large individual variations in respiratory motion and organ deformation. Hence, to estimate the 3D tumor region with only a mean deformation model would be difficult.

3.2.2. Statistical deformation model

Fig. 8 shows the deformation modes that correspond to the first two eigenvalues of the registered organ models. The eigenvalues and eigenvectors were computed from the set of displacement vectors of all vertices based on singular value decomposition. The central figures show the mean shape and mean displacement. The translucent shape is the end-inspiration phase ($t = 1$), and the opaque shape is the end-expiration phase ($t = 6$). The left/right images were generated by changing the weights to plus/minus σ, which is twice the square root of the eigenvalues.

The types of variety of motion and deformation can be characterized according to their morphological properties as follows:

- The first eigenvector mainly encompasses variation in the scale of deformation, which indicates that individual difference is large during the respiratory cycle.
- The second eigenvector is associated with the directions and rotations of deformation. Interestingly, the rotation axis and direction of rotation differ for each organ.

We also confirmed that the subspace representation using two eigenvectors explains 96.1% of the total deformation variation.

3.3. Deformation reconstruction performance

The aim of the next experiment was to investigate the prediction performance and characteristics of per-patient- and per-region-based learning models. For the experimental setup, 100 corresponding vertices were randomly sampled from each organ model, and a total of 500 vertices were used as multi-organ shape

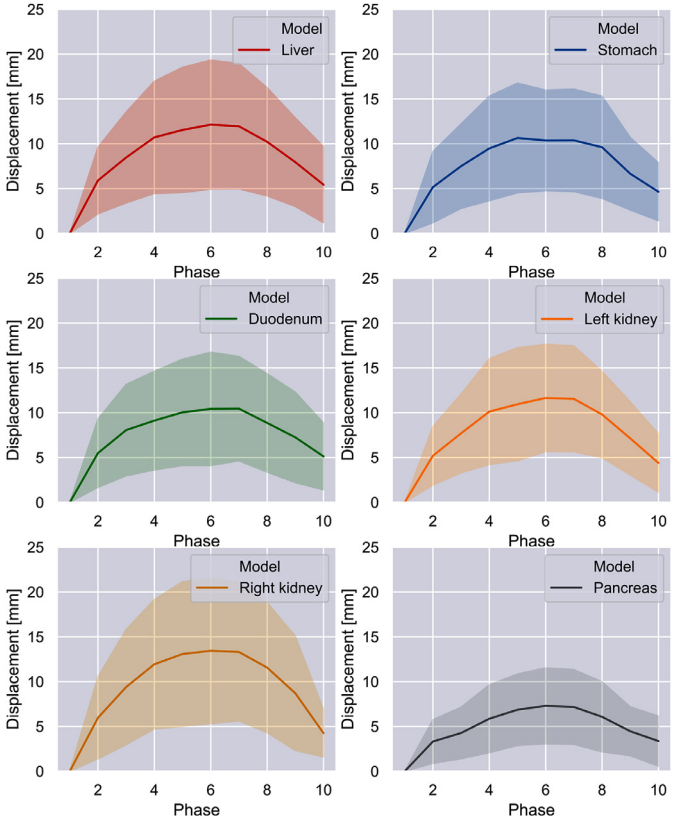

Fig. 7. Statistical motion dynamics of five abdominal organs and the GTV of pancreatic cancer. The means and standard deviations of the corresponding vertices are plotted in the graphs.

features, meaning that the dimensionality of the feature vector $\boldsymbol{x}$ was 3000. The displacement vectors of the GTV $\boldsymbol{y}$ were calculated using Eq. (1) through leave-one-out cross-validation. The per-patient- and per-region-based learning models were evaluated using the mean distance, Hausdorff distance, and Dice similarity coefficient between the estimated and ground truth regions of the pancreatic cancer. Fig. 9 shows box plots of the three error metrics for different weight parameter values. Significant differences were found for all the error metrics when using $10^{-5}, 10^{-4}, 0.001, 0.01, 0.1$ for the weight parameters by ANOVA ($p < 0.05$). The minimal estimation error was 6.0 ± 1.5 mm for per-patient-based learning, and 5.2 ± 1.3 mm for per-region-based learning, which shows that per-region-based learning improved the estimation performance by 13.4%.

The characteristics of the multidimensional feature sets depend on the complexity of the tumor localization problem and the number of data sets. These are both important factors affecting the estimation performance and the calculation cost. Therefore, we investigated the relationship between the estimation error of tumor localization and the number of sampling points N. A mean estimation error was calculated for ten trials of random sampling from five organs while increasing N from 1 to 400. The weight parameter of the kernel function was set to 3.0×10^{-5}, which results in good estimation performance.

Fig. 9 (d) shows the transition of the prediction performance of the two models. In the graph, per-region-based learning model shows consistently better prediction performance regardless of the number of sampling points. The estimation error decreased as the number of sampling points increased, and the error tends to converge over around 300 points. In the proposed per-region-based learning model, an average of 5.2 mm estimation error was achieved in the case of $N = 300$, which is a performance that is similar to the previous setting, which used 500 sampling points.

The estimation performance was also quantitatively compared to the conventional PCA-based, linear shape estimation approach

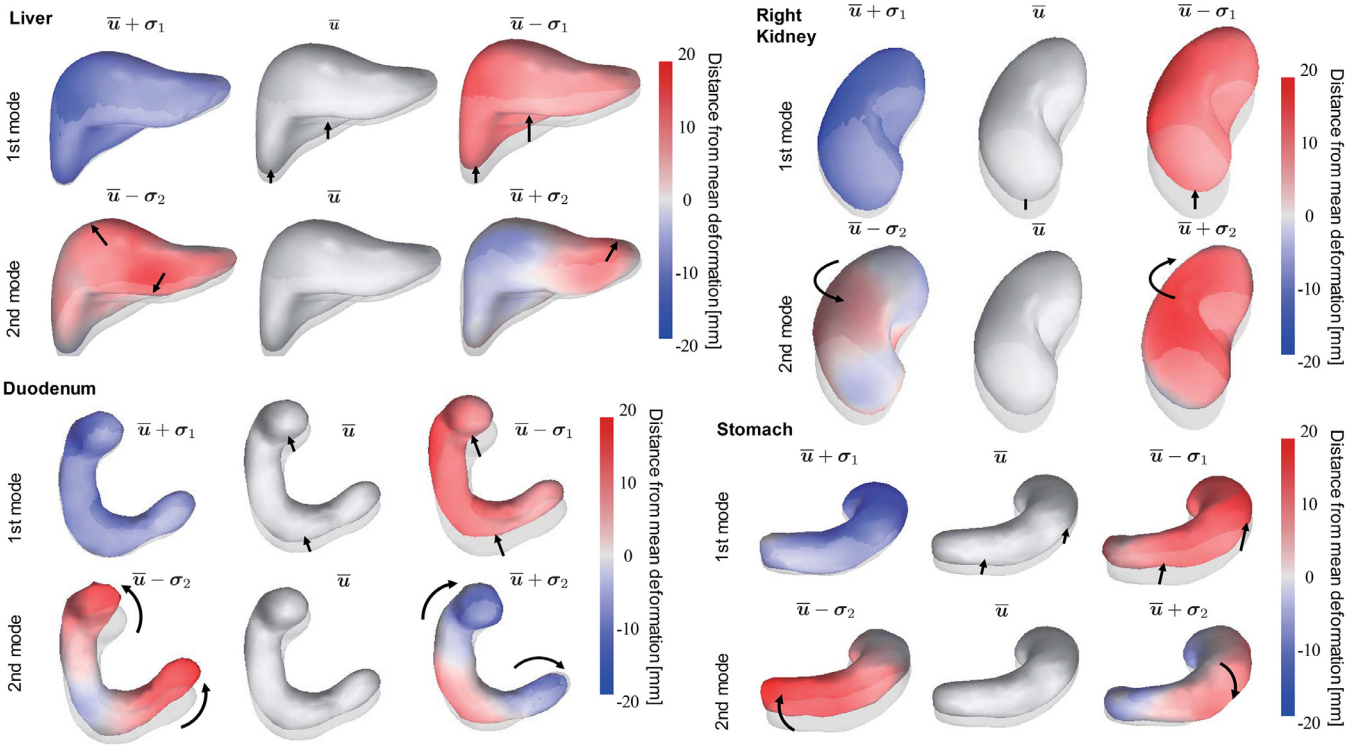

Fig. 8. Statistical deformation representation of the liver, stomach, duodenum, and right kidney. Deformation variations corresponding to the first two eigenvalues from the registered models are visualized. The color map shows the signed distance from the mean deformation.

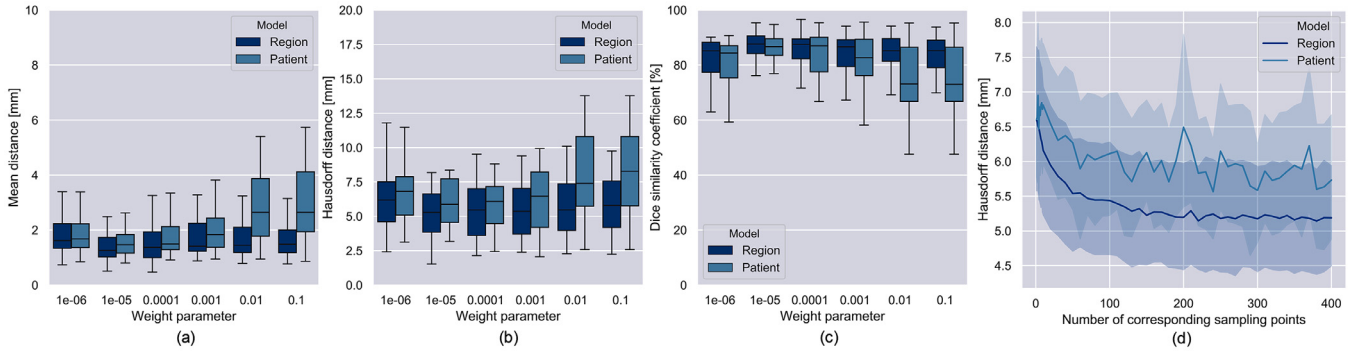

Fig. 9. Comparison of prediction performance between per-patient- and per-region-based learning. (a) mean distance, (b) Hausdorff distance, (c) Dice similarity coefficient and (d) estimation error of tumor localization with respect to the number of sampling points.

Table 3
Quantitative comparison of the estimation performance. The mean (minimum and maximum) values of mean distance (MD), Hausdorff distance (HD), and Dice similarity coefficient (DSC) for the PCA-based, per-patient-basis kernel, and proposed per-region-basis kernel model are reported.

	Methods		
	PCA	Kernel (per-patient)	Proposed (per-region)
MD [mm]	1.5 (0.8–3.4)	1.4 (0.7–4.3)	1.3 (0.6–2.8)
HD [mm]	6.1 (3.0–9.7)	5.8 (1.9–10.2)	4.9 (1.5–8.9)
DSC [%]	85.8 (67.2–93.2)	87.3 (66.1–93.5)	87.8 (68.0–96.8)

using five eigenvectors. On the basis of the subspace representation shown in the previous section, this number of dimensions was considered to be sufficient to cover the deformation variation in the dataset. For kernel-based models, the same parameters and the number of sampling points ($N = 300$) were used. Table 3 lists the median (minimum – maximum) values of MD, HD, and DSC. The per-patient-basis kernel model performed slightly better than the PCA-based model. The proposed per-region-basis model outperformed the other methods, and a significantly smaller Hausdorff distance was achieved (ANOVA, $p < 0.05$). These results suggest that the proposed concept could contribute to the stable deformation reconstruction of the GTV.

3.4. Multi-organ shape features

The investigation of effective feature sets in respiratory motion analysis is an important topic not only for kernel modeling but for deep learning applications. The next experiments confirm the relationship between 31 feature sets (all combinations of the five organs) and estimation accuracy in the prediction of pancreatic cancer deformation. This experiment also compares the results of the performance of the proposed multidimensional features and that of other regression approaches with a single organ or low-dimensional features. The number of sampling points was fixed to 300 based on the results of the previous experiments. For instance, when the liver and stomach are selected as feature sets, 150 points are randomly sampled from the liver and 150 points are randomly sampled from the stomach. Similarly, when all five organs are selected, 60 points are sampled from each organ.

Fig. 10 shows the median of the Hausdorff distance sorted in ascending order for 31 feature sets. These results suggest the following:

- Features from smaller organ sets show better estimation performance than ones sampled from all five organs.
- Estimations using only one organ tend to increase estimation error. Specifically, the right kidney leads to poor estimation performance.
- The stomach, duodenum, and left kidney are the best motion descriptors for estimating the deformable region of pancreatic cancer.

These findings suggest the validity of using the features of multiple neighboring organs rather than features sampled from the entire abdominal area. Shape features from the liver perform worse despite the fact that this organ is relatively close to the pancreas, but they are good candidates for feature descriptors when the contours of the stomach and duodenum are not available.

3.5. Estimation performance on motion dynamics

The goal of the motion/deformation analysis in this paper was to investigate the estimation performance of pancreatic cancer using multi-organ shape features. We analyzed the estimation error of GTV for ten time phases of the 4D-CT dataset, as shown

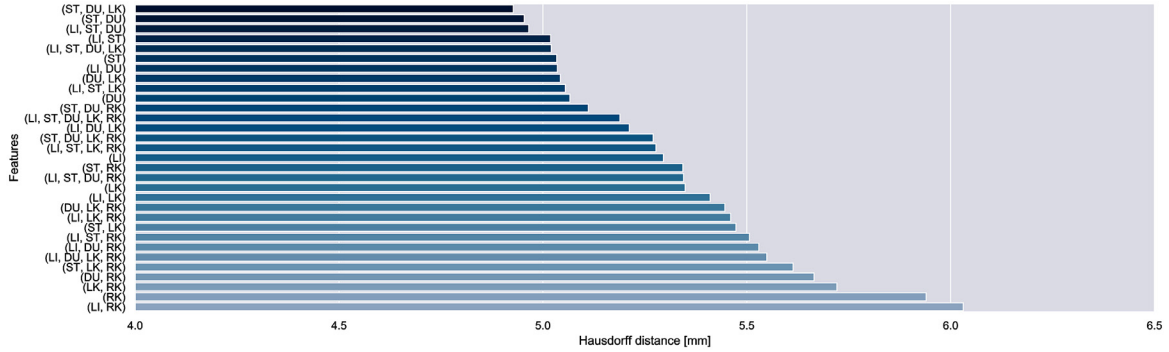

Fig. 10. Multi-organ shape features and prediction performance. LI: liver, ST: stomach, DU: duodenum, LK: left kidney, and RK: right kidney.

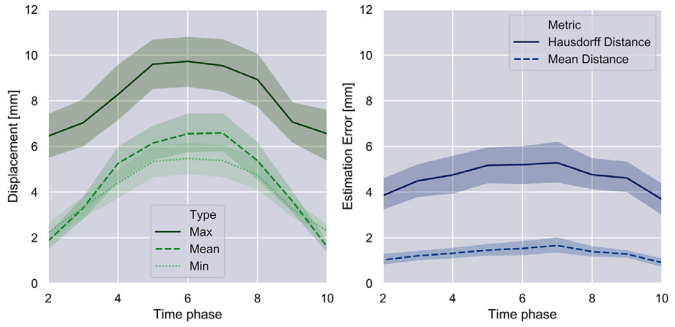

Fig. 11. Inter-patient variation of the GTV's motion with local deformation and estimation errors. (a) Mean, maximum, and minimum paths over one respiratory cycle, (b) The estimation error for ten time phases.

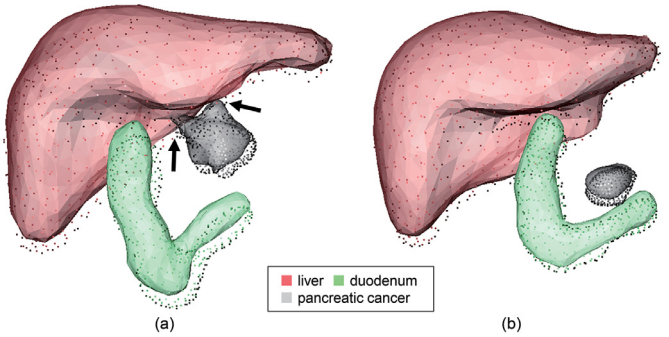

Fig. 12. Influence of surrounding organs on the surface displacement of the GTV. (a) Local deformations affected by the motion of the liver (indicated by the two arrows) and (b) translational motion with little deformation. The rendered surfaces are $t = 6$ and the points represent $t = 1$.

in Fig. 11. The analysis of the multi-organ feature sets show that, the stomach, duodenum, and left kidney were used for this prediction. The number of sampling points and parameters for the kernel models were the same as in the previous experiments. Fig. 11(a) shows the inter-patient variation of the GTV's motion with local deformation. The mean, maximum, and minimum path in one respiratory cycle are plotted as three lines, and each colored bandwidth is the standard deviation for 25-patient data. Because the displacement is calculated per vertex for the pancreas model, the difference between the maximum and minimum paths represents a local deformation exceeding 5 mm on average. The overall path also includes considerable variations with over 10 mm differences in individual respiratory motion. This can also be confirmed in the full bandwidth of Fig. 7.

The transition of the estimation error for ten time phases using the designed kernel model is plotted in Fig. 11(b). Despite the inter-patient variation of motion and deformation observed in Fig. 11(a), the mean $\pm$ standard deviation of the distance was 1.2 $\pm$ 0.7 mm and that of the Hausdorff distance was 4.2 $\pm$ 2.3 mm. Both errors remained small throughout the respiration. These results suggest that the GTV can be adequately localized by the shape features of the surrounding organs, specifically the stomach, duodenum, and left kidney, even if the pancreas is not directly detected.

In several cases, we confirmed that when the GTV is close to the liver, its local shape is strongly affected by the motion/deformation of the liver. In contrast, when the GTV is located near the lower abdomen or duodenum, local deformation is relatively small and close to simple translational motion. Fig. 12 shows the two cases in which this tendency is shown. This may happen because of the difference in stiffness and local deformation of the surrounding organs. The smaller HD demonstrates that these two different displacements could be stably predicted by the feature sets (liver, stomach, and duodenum) obtained in our experiment.

We measured the computation time needed to predict the GTV deformation reconstruction from multi-organ features. The overall computation time for predicting GTV motion/deformation was 47–48 s for one patient. Because kernel matrix K and optimized weights α are determined from the registered mesh database in advance, online prediction can be achieved by computing the matrix-vector multiplication in Eq. (6).

4. Discussion

To our knowledge, this study is the first to build a statistical multi-organ deformation library of five abdominal organs that includes inter- and intra-patient shape variations. Image-based deformable registration (Sotiras et al., 2013; Oh and Kim, 2017) is a popular approach for deformed bodies, however, matching multi-organ regions tends to result in large registration errors, especially around the organ boundaries. The potential of DMR has recently been rediscovered (Rigaud et al., 2019; Magallon-Baro et al., 2019; Nakamura et al., 2019), and the proposed LDSM for each organ address problems with matching organs with rotational components and sliding boundaries. Moreover, it achieved stable registration with a Hausdorff distance error of less than 1 mm. We note that this result outperforms the registration error of 3.1–3.3 mm reported for the SSM of CTV of the cervix–uterus and bladder in recent work (Rigaud et al., 2019).

In the latter part of this paper, the application of the proposed deformation library to time-series deformation reconstruction of GTV (i.e., pancreatic cancer) was presented. Regarding studies that focus on related approaches, Wilms et al. (2017) recently proposed multi-resolution multi-object statistical models and showed their performance on standard shape modeling problems. Geimer et al. (2017) developed a kernel-based framework for the respiratory motion estimation of lungs. In this study, we proposed a localized deformation learning model for five abdominal organs, and investigated effective shape features for the kernel regression of GTV motion. Despite this study's limited data size, the results showed that stable estimation could be achieved throughout the respiration cycle. The findings and the developed database will be useful for determining the planning target volume of pancreatic cancer from the available features of the surrounding organs.

Table 3 shows that the minimal value of the DSC does not change much between the methods. A linear relationship between the GTV and surrounding organs can be modeled by PCA, and the location (or the center of magnitude) of the GTV was well estimated by all three methods. However, in some cases such as that in Fig. 12(a), relatively large, local deformation was confirmed. This happens because the GTV is close to or neighboring the liver, and the liver deforms with rotational motion. Because PCA is a linear model, it fails to represent such complex, non-linear deformation due to the influence of the liver motion, and local shape errors become large. We believe that such non-linear deformation was the main reason why the minimum value of DSC does not change much despite the changes in maximum value. Moreover, in HD, a relatively large difference was confirmed.

To clarify the focus of this research, the spatial displacement of the internal structures of the mesh was considered to be outside the scope of this paper. This is because the assumed application is radiotherapy planning, in which the 3D contour (i.e., surface) of the GTV and OARs must be estimated. Because the developed library uses a tetrahedral mesh in the DMR and can express internal deformation, we consider that further modeling and evaluation of internal structures would be possible in future work.

We assume that the clinical application of the proposed techniques exists in two scenarios. One is when adapting the precomputed treatment plan to the "motion of the day". The results showed that the GTV motion can be estimated from sparsely-sampled points of the five organs. It is difficult to stably obtain a clear anatomical contour because of defects or artifacts in CBCT images. Especially in deep organs around pancreatic cancer, feature acquisition becomes even more unstable. However, it is possible to sample local textures or partial image features from surrounding organs such as the liver, and our framework does not require a complete anatomical contour for deformation estimation. Sparse features sampled from the visible portion of the surrounding organs are available as good estimators to reconstruct the 3D contour of the GTV and OARs. Thus, the developed framework does not assume dense, high-quality 4D-CT images and would be able to perform deformation/motion estimation from lower-quality images measured during the treatment period. We believe that the ability to estimate tumor displacement based on clearly visible information can improve stability of prediction during ART.

The second clinical scenario is to apply the developed multi-organ library to markerless radiation in tumor-tracking radiotherapy. Some recent studies have reported pixel-to-shape techniques, i.e., 3D shape/deformation reconstruction from a single 2D image (Wang et al., 2019; Wu et al., 2019; Nakao et al., 2017). The respiratory motion between the lung and the surrogate has also been modeled (Geimer et al., 2017). With these techniques, real-time tumor localization may be possible from measured time-series X-ray images or surrogate motion during actual intervention. However, technical issues still lie in the accuracy of their shape reconstruction, especially in the abdominal region. The developed deformation library and extracted multi-organ feature sets would improve their estimation accuracy and clinical applicability. Combining such 3D reconstruction techniques with statistical deformation models will be our future work.

5. Conclusion

In this paper, we introduced a multi-organ deformation library and its application to pancreatic cancer localization based on the shape features of multiple organs. The statistical multi-organ motion/deformation library of the stomach, liver, left and right kidneys, and duodenum was generated by the DMRs of their organ meshes generated from 4D-CT images (250 volumes). The proposed LDSM method achieved stable registration with a Hausdorff distance error of less than 1 mm. Per-region-based deformation learning using kernel regression was also proposed to predict the displacement of pancreatic cancer for ART. The experiment results show that the proposed concept better estimates, and achieves a clinically acceptable estimation error for mean distance (1.2 ± 0.7 mm) and the Hausdorff distance (4.2 ± 2.3 mm) throughout the respiratory motion.

Declaration of Competing Interest

The authors declare that they have no known competing financial interests or personal relationships that could have appeared to influence the work reported in this paper.

CRediT authorship contribution statement

Megumi Nakao: Conceptualization, Methodology, Software, Visualization, Writing - original draft. **Mitsuhiro Nakamura:** Data curation, Investigation, Validation, Writing - review & editing. **Takashi Mizowaki:** Resources, Supervision. **Tetsuya Matsuda:** Supervision, Validation, Writing - review & editing.

Acknowledgments

This research was supported by JSPS Grant-in-Aid for Scientific Research (B) (grant number 18H02766 and 19H04484). A part of this study was also supported by a JSPS Grant-in-Aid for challenging Exploratory Research (grant number 18K19918). We thank Taiji Iwai for supporting preliminary experiments. We thank Kimberly Moravec, Ph.D., from Edanz Group (www.edanzediting.com/ac) for editing a draft of this manuscript.

Supplementary material

Supplementary material associated with this article can be found, in the online version, at doi:10.1016/j.media.2020.101829.

References

Beg, M.F., Miller, M.I., Trouvé, A., Younes, L., 2005. Computing large deformation metric mappings via geodesic flows of diffeomorphisms. Int. J. Comput. Vis. 61 (2), 139–157.
Bondar, L., Intven, M., Burbach, J.P., Budiarto, E., Kleijnen, J.P., Philippens, M., van Asselen, B., Seravalli, E., Reerink, O., Raaymakers, B., 2014. Statistical modeling of CTV motion and deformation for IMRT of early-stage rectal cancer. Int. J. Radiat. Oncol. Biol. Phys. 90 (3), 664–672.
Ehrhardt, J., Werner, R., Schmidt-Richberg, A., Handels, H., 2011. Statistical modeling of 4D respiratory lung motion using diffeomorphic image registration. IEEE Trans. Med. Imaging 30 (2), 251–265.
Fontana, G., Riboldi, M., Gianoli, C., Chirvase, C.I., Villa, G., Paganelli, C., Summers, P.E., Tagaste, B., Pella, A., Fossati, P., Ciocca, M., Baroni, G., Valvo, F., Orecchia, R., 2016. MRI quantification of pancreas motion as a function of patient setup for particle therapy - a preliminary study. J. Appl. Clin. Med. Phys. 17 (5), 60–75.
Fuerst, B., Mansi, T., Carnis, F., Sälzle, M., Zhang, J., Declerck, J., Boettger, T., Bayouth, J., Navab, N., Kamen, A., 2015. Patient-specific biomechanical model for the prediction of lung motion from 4-D CT images. IEEE Trans. Med. Imaging 34 (2), 599–607.
Geimer, T., Unberath, M., Birlutiu, A., Taubmann, O., Wolfelschneider, J., Bert, C., Maier, A., 2017. A kernel-based framework for intra-fractional respiratory motion estimation in radiation therapy. pp. 1036–1039.
Haekal, M., Arimura, H., Hirose, T.A., Shibayama, Y., Ohga, S., Fukunaga, J., Umezu, Y., Honda, H., Sasaki, T., 2018. Computational analysis of interfractional anisotropic shape variations of the rectum in prostate cancer radiation therapy. Phys. Med. Biol. 46, 168–179.
Heimann, T., Meinzer, H.P., 2009. Statistical shape models for 3D medical image segmentation: A review. Med. Image Anal. 13 (4), 543–563.
Huttenlocher, D.P., Klanderman, G.A., Rucklidge, W.A., 1993. Comparing images using the Hausdorff distance. IEEE Trans. Pattern Anal. Mach. Intell. 15 (9), 850–863.
Hvid, C.A., Elstrom, U.V., Jensen, K., Grau, C., 2018. Cone-beam computed tomography (CBCT) for adaptive image guided head and neck radiation therapy. Acta Oncol. 57 (4), 552–556.
Iwai, T., Nakao, M., Nakamura, M., Matsuda, T., 2017. A tracking method of invisible tumors using surrounding features on time series X-ray images. Int. J. Comput. Assist. Radiol. Surg. 12 (1), S206–S207.
Jadon, R., Pembroke, C.A., Hanna, C.L., Palaniappan, N., Evans, M., Cleves, A.E., Staffurth, J., 2014. A systematic review of organ motion and image-guided strategies in external beam radiotherapy for cervical cancer. Clin. Oncol. 26 (4), 185–196.
Jud, C., Giger, A., Sandkühler, R., Cattin, P.C., 2017. A localized statistical motion model as a reproducing kernel for non-rigid image registration. In: Medical Image Computing and Computer-Assisted Intervention (MICCAI), pp. 261–269.
Kim, J., Valdes-Hernandez Mdel, C., Royle, N.A., Park, J., 2015. Hippocampal shape modeling based on a progressive template surface deformation and its verification. IEEE Trans. Med. Imaging 34 (6), 1242–1261.
Klein, S., Staring, M., Murphy, K., Viergever, M.A., Pluim, J.P., 2010. Elastix: a toolbox for intensity-based medical image registration. IEEE Trans. Med. Imaging 29 (1), 196–205.
Magallon-Baro, A., Loi, M., Milder, M.T.W., Granton, P.V., Zolnay, A.G., Nuyttens, J.J., Hoogeman, M.S., 2019. Modeling daily changes in organ-at-risk anatomy in a cohort of pancreatic cancer patients. Radiother. Oncol. 134, 127–134.
Nakamura, M., Nakao, M., Hirashima, H., Iramina, H., Mizowaki, T., 2019. Performance evaluation of a newly developed three-dimensional model-based global-to-local registration in prostate cancer. J. Radiat. Res. 60 (5), 595–602.
Nakao, M., Kawashima, A., Kokubo, M., Minato, K., 2007. Simulating lung tumor motion for dynamic tumor-tracking irradiation. In: IEEE Nuclear Science Symposium and Medical Imaging Conference (NSS-MIC), 6, pp. 4549–4551.
Nakao, M., Minato, K., 2010. Physics-based interactive volume manipulation for sharing surgical process. IEEE Trans. Inf. Technol. Biomed. 14 (3), 809–816.
Nakao, M., Saito, A., Matsuda, T., 2017. A simulation study on deformation estimation of elastic materials using monocular images. Int. J. Comput. Assist. Radiol. Surg. 12 (1), S257–S258.

Nakao, M., Tokuno, J., Chen-Yoshikawa, T., Date, H., Matsuda, T., 2019. Surface deformation analysis of collapsed lungs using model-based shape matching. Int. J. Comput. Assist. Radiol. Surg. 14 (10), 1763–1774.
Nealen, A., Igarashi, T., Sorkine, O., Alexa, M., 2006. Laplacian mesh optimization. In: Proc. of 4th Int. Conf. on Computer Graphics and Interactive Techniques, pp. 381–389.
Oh, S., Kim, S., 2017. Deformable image registration in radiation therapy. Radiat. Oncol. J. 35 (2), 101–111.
Pitiot, A., Bardinet, E., Thompson, P.M., Malandain, G., 2006. Piecewise affine registration of biological images for volume reconstruction. Med. Image Anal. 10 (3), 465–483.
Posiewnik, M., Piotrowski, T., 2019. A review of cone-beam CT applications for adaptive radiotherapy of prostate cancer. Phys. Med. 59, 13–21.
Rigaud, B., Simon, A., Gobeli, M., Leseur, J., Duverge, L., Williaume, D., Castelli, J., Lafond, C., Acosta, O., Haigron, P., De Crevoisier, R., 2019. Statistical shape model to generate a planning library for cervical adaptive radiotherapy. IEEE Trans. Med. Imaging 38 (2), 406–416.
Robert, K., Anthony, J.P., Reith, S., Josephine, T., Katherine, E.F., Neil, P., Daniel, S., James, D.M., Todd, F.A., 2017. Correlation of liver and pancreas tumor motion with normal anatomical structures determined with deformable image registration. Biomed. Phys. Eng. Exp. 3 (1), 017001.
Ruhaak, J., Polzin, T., Heldmann, S., Simpson, I.J.A., Handels, H., Modersitzki, J., Heinrich, M.P., 2017. Estimation of large motion in lung CT by integrating regularized keypoint correspondences into dense deformable registration. IEEE Trans. Med. Imaging 36 (8), 1746–1757.
Saito, A., Nakao, M., Uranishi, Y., Matsuda, T., 2015. Deformation estimation of elastic bodies using multiple silhouette images for endoscopic image augmentation. In: IEEE Int. Symp. on Mixed and Augmented Reality, pp. 170–171.
Shibayama, Y., Arimura, H., Hirose, T.A., Nakamoto, T., Sasaki, T., Ohga, S., Matsushita, N., Umezu, Y., Nakamura, Y., Honda, H., 2017. Investigation of interfractional shape variations based on statistical point distribution model for prostate cancer radiation therapy. Med. Phys. 44 (5), 1837–1845.
Soliman, A., Khalifa, F., Elnakib, A., Abou El-Ghar, M., Dunlap, N., Wang, B., Gimel'farb, G., Keynton, R., El-Baz, A., 2017. Accurate lungs segmentation on CT chest images by adaptive appearance-guided shape modeling. IEEE Trans. Med. Imaging 36 (1), 263–276.
Sotiras, A., Davatzikos, C., Paragios, N., 2013. Deformable medical image registration: a survey. IEEE Trans. Med. Imaging 32 (7), 1153–1190.
Teske, H., Mercea, P., Schwarz, M., Nicolay, N.H., Sterzing, F., Bendl, R., 2015. Real–time markerless lung tumor tracking in fluoroscopic video: Handling overlapping of projected structures. Med. Phys. 42 (5), 2540–2549.
Tilly, D., van de Schoot, A.J.A.J., Grusell, E., Bel, A., Ahnesjo, A., 2017. Dose coverage calculation using a statistical shape model applied to cervical cancer radiotherapy. Phys. Med. Biol. 62 (10), 4140–4159.
Wang, Y., Zhong, Z., Hua, J., 2019. Deeporgannet: on-the-fly reconstruction and visualization of 3D/4D lung models from single-view projections by deep deformation network. arXiv preprint.
Whitfield, G., Jain, P., Green, M., Watkins, G., Henry, A., Stratford, J., Amer, A., Marchant, T., Moore, C., Price, P., 2012. Quantifying motion for pancreatic radiotherapy margin calculation. Radiother. Oncol. 103 (3), 360–366.
Wilms, M., Ha, I.Y., Handels, H., Heinrich, M.P., 2016. Model-based regularisation for respiratory motion estimation with sparse features in image-guided interventions. In: Medical Image Computing and Computer-Assisted Intervention (MICCAI), pp. 89–97.
Wilms, M., Handels, H., Ehrhardt, J., 2017. Multi-resolution multi-object statistical shape models based on the locality assumption. Med. Image Anal. 38, 17–29.
Wu, S., Nakao, M., Tokuno, J., Chen-Yoshikawa, T., Matsuda, T., 2019. Reconstructing 3D lung shape from a single 2D image during the deaeration deformation process using model-based data augmentation. In: IEEE Int. Conf. on Biomedical and Health Informatics (BHI), pp. 1–4.
Xu, X., Zhou, F., Liu, B., Fu, D., Bai, X., 2019. Efficient multiple organ localization in CT image using 3D region proposal network. IEEE Trans. Med. Imaging 38 (8), 1885–1898.
Yu, A., Woo, S.M., Joo, J., Yang, H.-R., Lee, W.J., Park, S.-J., Nam, B.-H., 2016. Development and validation of a prediction model to estimate individual risk of pancreatic cancer. PLoS One 11 (1), e0146473.
Zhang, D., Chen, K., 2018. A novel diffeomorphic model for image registration and its algorithm. J. Math. Imaging Vis. 60 (8), 1261–1283.
Zhou, J., Kim, S., Jabbour, S., Goyal, S., Haffty, B., Chen, T., Levinson, L., Metaxas, D., Yue, N.J., 2010. A 3D global-to-local deformable mesh model based registration and anatomy-constrained segmentation method for image guided prostate radiotherapy. Med. Phys. 37 (3), 1298–1308.